

Motion-Adaptive Spatio-Temporal Regularization (MASTeR) for Accelerated Dynamic MRI

M. Salman Asif^{1,*}, Lei Hamilton¹, Marijn Brummer², Justin Romberg¹

¹School of Electrical and Computer Engineering, Georgia Institute of Technology, Atlanta, Georgia, USA

²Echogenix, LLC, Dunwoody, Georgia, USA

*Corresponding author:

M. Salman Asif

E-mail: sasif@gatech.edu

Georgia Institute of Technology

School of Electrical and Computer Engineering

5254-W Centergy Building

75 Fifth Street NW

Atlanta, GA 30308

Approximate word count: 160 (abstract) 4900 (body)

Running head: MASTeR

Revised manuscript submitted to *Magnetic Resonance in Medicine* as a Full Paper.

This work was supported by ONR grant N00014-08-0884 and a grant from the Packard Foundation.

Abstract

Accelerated MRI techniques reduce signal acquisition time by undersampling k-space. A fundamental problem in accelerated MRI is the recovery of quality images from undersampled k-space data. Current state-of-the-art recovery algorithms exploit the spatial and temporal structures in underlying images to improve the reconstruction quality. In recent years, compressed sensing theory has helped formulate mathematical principles and conditions that ensure recovery of (structured) *sparse* signals from undersampled, *incoherent* measurements. In this paper, a new recovery algorithm, motion-adaptive spatio-temporal regularization (MASTeR), is presented. MASTeR, which uses compressed sensing principles to recover dynamic MR images from highly undersampled k-space data, takes advantage of spatial and temporal structured sparsity in MR images. In contrast to existing algorithms, MASTeR models temporal sparsity using motion-adaptive linear transformations between neighboring images. The efficiency of MASTeR is demonstrated with experiments on cardiac MRI for a range of reduction factors. Results are also compared with k-t FOCUSS with motion estimation and compensation—another recently proposed recovery algorithm for dynamic MRI.

Key words: Compressed sensing, sparse representation, ℓ_1 -norm minimization, spatial and temporal regularization, motion estimation and motion compensation.

Introduction

Magnetic resonance imaging (MRI) is a versatile and highly accurate imaging modality. Although MRI is used to diagnose numerous medical conditions, current technology has several practical limitations, one of which is slow imaging speed. Imaging speed in MRI is limited by physical and physiological constraints associated with rapidly switching magnetic field gradients. Lack of speed poses particular challenges for applications in dynamic cardiac MRI. To reduce artifacts related to respiratory motion, most routine cardiac MRI techniques acquire images during a patient’s breath-holds. In fact, a complete acquisition takes a few cardiac cycles and may require multiple breath-holds by the patient. Thus, the patient’s ability to sustain breath-holds along with imaging speed determine the duration of the examination, which in turn, determines the spatial and temporal resolution of the images. However, since many patients are unable to sustain breath-holds, the acquisition process must be accelerated to reduce scan time.

With the introduction of reduced-data imaging methods, reduction in the scan time does not require an increase in imaging speed (via enhanced gradient performance), but instead, a reduction in the number of phase-encoding lines that results in an undersampled k-space. A fundamental challenge in reduced-data imaging is to recover high-resolution images from undersampled k-space data, a problem that is often underdetermined. One common approach to solve such an underdetermined problem is to utilize the spatial and temporal structures in the images and the redundancies in the acquisition setup.

In this paper, we present a new recovery algorithm for highly accelerated dynamic MRI with multiple receiver coils. To recover high-resolution images from undersampled k-space data, our algorithm exploits spatial and temporal structured sparsity in MR images. To model spatial sparsity, we use wavelet transform. To model temporal sparsity, we use inter-frame motion, which is a useful tool for representing temporal variations in video frames. In our recovery setup, we treat the underlying image sequence as a group of video frames in which an image can be predicted from its neighboring images through a motion-adaptive interpolation. The difference between an original image and its motion-adaptive interpolation is called a motion-compensated residual, which often provides a (structured) sparse image. The recovery algorithm solves a convex optimization problem that involves cost functions for data mismatch, spatial sparsity of each image, and temporal sparsity of motion-compensated residuals. To promote spatial and temporal structured sparsity in the solution, we use the ℓ_1 -norm regularization. We call this method *motion-adaptive spatio-temporal regularization* (MASTeR).

Based on different sources of prior information, current state-of-the-art methods for dynamic MRI can be categorized as follows: parallel imaging methods, reduced field of view methods, compressed sensing-based methods, and a combination of these methods that can use multiple independent sources of prior information.

Parallel imaging methods such as SENSE (1), SPACE-RIP (2), SMASH (3), and GRAPPA (4) utilize information provided by multiple receiver coils and recover images from undersampled k-space data provided by each receiver. The main idea behind reduced field of view (rFOV) methods such as UNFOLD (5) and Noquist (6) is to exploit the spatiotemporal redundancy that is often available in dynamic imaging because parts of the field of view remain static over time. Parallel imaging and rFOV methods utilize independent prior information sources to accelerate imaging speed and they can be combined for even higher acceleration or reduced image artifacts. Examples of methods that integrate parallel imaging with rFOV are TSENSE (7), k-t SENSE (8), and PINOT (9).

A recent addition to reduced-data imaging is compressed sensing (CS)-based methods (10, 11, 12, 13, 14). CS theory has shown that, under certain conditions, a *sparse* signal can be recovered from a small number of linear, incoherent measurements (15, 16). However, signal recovery from the resulting underdetermined system involves solving an optimization problem (17, 18). An effective convex optimization program, which comes with various theoretical guarantees, minimizes the ℓ_1 -norm of the sparse signal under some data-fidelity constraints (19, 20). Sparse MRI (10) exploits spatial sparsity in MR images, such as sparsity of angiography images in the image domain and sparsity of brain or cardiac images in the wavelet or total-variation domain. CS-SENSE (12) and SparseSENSE (11) combine parallel imaging with CS. k-t SPARSE (21) and k-t FOCUSS (13) use a temporal discrete Fourier transform (DFT) for sparse representation of temporal variations in cardiac images. k-t FOCUSS can also be used with data-driven transforms such as Karhunen-Loeve transform or principle component analysis.

The rFOV (with static and dynamic partition) and temporal-DFT methods use *fixed* transforms along straight lines in the temporal direction without taking spatial dependencies into account. For every pixel location, these methods impose a model that does not use (nor does it provide) any information about neighboring pixels within the same frame or across different frames. However, variations in dynamic MR images arise because physical changes occur over time. For instance, a scan of a beating heart reveals different states of the heart in a cardiac cycle. Intensities of pixels overlapping the heart wall change as the heart beats (possibly in a near-periodic fashion), but at the same time, the wall of the heart changes its position from one frame to the next. These changes, correlated in both space and time, appear as a displacement of pixels in images and provide direct information about the temporal structure in the image sequence. The displacement of pixels in a sequence of images is commonly referred to as inter-frame motion, which plays a fundamental role in modern video compression (e.g., in H.264 and MPEG standards) (22, 23). Inter-frame motion provides an efficient and direct representation for variations as well as dependencies in a sequence of closely-related images.

k-t FOCUSS with motion estimation/motion compensation (ME/MC) (13, 24) is another recently proposed method for dynamic MRI that uses inter-frame motion during the recovery process.

k-t FOCUSS with ME/MC reconstructs motion-compensated residuals of the entire image sequence with respect to a reference image by assuming that the residuals have sparse temporal-DFT. To estimate the inter-frame motion, k-t FOCUSS with ME/MC recommends using a fully sampled image as a reference frame. In the absence of a fully-sampled image, a reference image can be generated from the temporal average of k-t measurements for the entire image sequence or for only those images that correspond to the diastole phase, where the latter approach would reduce blurring in the reference image. The quality of reconstruction for k-t FOCUSS with ME/MC directly depends on the quality of the reference image and the accuracy with which it can model the true motion-compensated residuals.

The main contribution of this paper is the use of motion-adaptive transforms that model temporal dependencies between adjacent images in both forward and backward directions. Our model can be interpreted as a linear dynamical system in which neighboring images are linked through a motion-adaptive transform that interpolates pixel values of an image to a new set of locations described by the inter-frame motion. In contrast to k-t FOCUSS with ME/MC, our proposed method, MASTeR, does not require any reference frame. Instead, all the inter-frame dependencies are embedded in the linear dynamical system formulation. As a result, it provides a practical and versatile recovery scheme that combines parallel imaging with spatial and temporal regularization in a unified manner. MASTeR consists of two main steps: initialization and motion adaptation. The initialization step estimates the image sequence without any motion information. The motion-adaptation step, which can be repeated multiple times, estimates inter-frame motion in the reconstructed images and applies it to further refine image estimates. Experiments demonstrate that our method provides good reconstructed MR images from highly undersampled k-space measurements. A comparison with k-t FOCUSS with ME/MC (13) shows that MASTeR reconstructs images with a better spatio-temporal resolution, a better signal-to-noise ratio, and fewer artifacts.

Theory

Imaging model

Consider a dynamic MRI setup in which data consist of T images in a cardiac cycle. The vector form of the imaging system for an i^{th} image can be written as

$$\mathbf{y}_i = \mathcal{A}_i \mathbf{x}_i + \mathbf{e}_i, \quad [1]$$

where \mathbf{x}_i is an N -length vector that denotes the underlying two-dimensional complex-valued MR image, \mathbf{y}_i denotes a vector with k -space measurements of \mathbf{x}_i , and \mathbf{e}_i denotes noise in the measurements. Encoding matrix \mathcal{A}_i consists of Fourier transform coefficients weighted by coil sensitivity maps. Suppose the system has C receiver coils and at time i we receive M k-space samples from

every coil at locations specified by set Ω_i . The expanded form of \mathcal{A}_i in Eq. 1 can be written as

$$\mathcal{A}_i \equiv \begin{bmatrix} \mathcal{F}_{\Omega_i} S_i^1 \\ \vdots \\ \mathcal{F}_{\Omega_i} S_i^C \end{bmatrix}, \quad [2]$$

where S_i^1, \dots, S_i^C denote the sensitivity profiles of C receiver coils and \mathcal{F}_{Ω_i} denotes an operator that computes Fourier coefficients only at locations indexed by set Ω_i . We can write the overall dynamic MRI system as follows:

$$\begin{bmatrix} \mathbf{y}_1 \\ \mathbf{y}_2 \\ \vdots \\ \mathbf{y}_T \end{bmatrix} = \begin{bmatrix} \mathcal{A}_1 & 0 & \dots & 0 \\ 0 & \mathcal{A}_2 & \dots & 0 \\ \vdots & \vdots & \ddots & \vdots \\ 0 & 0 & \dots & \mathcal{A}_T \end{bmatrix} \begin{bmatrix} \mathbf{x}_1 \\ \mathbf{x}_2 \\ \vdots \\ \mathbf{x}_T \end{bmatrix} + \begin{bmatrix} \mathbf{e}_1 \\ \mathbf{e}_2 \\ \vdots \\ \mathbf{e}_T \end{bmatrix} \quad [3]$$

$$\equiv \mathbf{y} = \mathcal{A}\mathbf{x} + \mathbf{e},$$

where \mathbf{x} denotes a vector of length TN (with all of the T images stacked on top of each other), \mathbf{y} is a vector of length TCM (consisting of all the k-space measurements), \mathcal{A} is a $TCM \times TN$ system matrix, and \mathbf{e} denotes noise in the measurements. We call $R = N/M$ the reduction factor or acceleration factor.

In accelerated MRI, increasing the acceleration factor (R) causes the system in Eq. 3 to become highly ill-conditioned and eventually underdetermined. To recover the underlying images from such an underdetermined system, we need additional information about the structure of the underlying images. A comprehensive theory that addresses such problems is compressed sensing.

Structure and recovery

Compressed sensing theory provides a general sensing and reconstruction framework in which a *sparse* signal can be recovered from a small number of linear, *incoherent* measurements (15, 16). It is a well-known fact that most natural signals inherently contain redundant information that can be represented using a small number of important features. For example, images can be represented using a small number of discrete cosine transform (DCT) or wavelet transform coefficients; adjacent frames in a video can be represented using a reference frame and motion-compensated residuals. In principle, CS schemes use such prior information about sparse structures to enable the recovery of signals from a small number of measurements. The recovery process involves solving an optimization problem that promotes the desired structure in the solution while maintaining fidelity towards the measurements. An example of such an optimization program is the following ℓ_1 -regularized least-

squares problem:

$$\underset{\mathbf{x}}{\text{minimize}} \underbrace{\|\mathcal{A}\mathbf{x} - \mathbf{y}\|_2^2}_{\text{data fidelity}} + \tau \underbrace{\|\Theta\mathbf{x}\|_1}_{\text{structure}}, \quad [4]$$

where the ℓ_2 term keeps the solution close to the measurements, the ℓ_1 term encourages the solution to be sparse with the Θ transform, and $\tau > 0$ is the so-called regularization parameter that controls the tradeoff between data fidelity and signal sparsity.

CS principles can be easily applied to the dynamic MRI because MR images exhibit sparsity in a variety of spatial transforms along with significant redundancies in the temporal direction. Moreover, to satisfy the incoherence requirement of the CS system, k-space measurements for each frame can be selected at random (e.g., uniform or variable-density phase-encoded sampling) (10). To extract the best results from the least number of measurements, a recovery algorithm must exploit both the spatial and temporal structures in MR images. Previous applications of CS in dynamic MRI have used spatial transform sparsity (10, 11, 12) as well as temporal transform sparsity (21, 25, 13) in MR images. In the rest of this section, we summarize several state-of-the-art recovery methods that use the spatial and temporal structures of MR images.

We start our discussion with the simple least squares (LS) formulation in which we will later add regularization terms that promote certain desired structures in the reconstructed signals. The LS method—one of the simplest algorithms for MR image recovery—minimizes the data mismatch without assuming any specific structure in the signal. If \mathcal{A} in Eq. 3 has full column rank, \mathbf{x} can be reliably estimated by solving the following LS problem:

$$\underset{\mathbf{x}}{\text{minimize}} \sum_i \|\mathcal{A}_i \mathbf{x}_i - \mathbf{y}_i\|_2^2. \quad [5]$$

The problem in Eq. 5 can be solved separately for each \mathbf{x}_i (26). However, if \mathcal{A} becomes ill-conditioned or underdetermined, the LS method does not provide a reliable solution (10), necessitating the use of additional information in the recovery process.

MR images exhibit spatial sparsity in a variety of transforms such as wavelets and finite differences. In the CS framework, we can easily incorporate spatial sparsity in the recovery process by adding a new regularization term to Eq. 5. One candidate is the following convex program:

$$\underset{\mathbf{x}}{\text{minimize}} \sum_i \|\mathcal{A}_i \mathbf{x}_i - \mathbf{y}_i\|_2^2 + \tau \|\Psi \mathbf{x}_i\|_1, \quad [6]$$

where Ψ denotes a sparsity inducing transform applied to each image. The program in Eq. 6 can also be solved using a variety of fast and efficient solvers (27, 28, 29, 30, 31).

In dynamic MRI, significant gains can be achieved by exploiting the temporal structure across different images in the sequence (32, 14). A number of recently proposed methods for cardiac MRI use Fourier transform to model sparsity in the temporal direction (21, 8, 13). An example of a

recovery program that incorporates a temporal DFT can be written as

$$\underset{\mathbf{x}}{\text{minimize}} \|\mathcal{A}\mathbf{x} - \mathbf{y}\|_2^2 + \lambda \|\mathcal{F}_t\mathbf{x}\|_1, \quad [7]$$

where $\mathcal{F}_t\mathbf{x}$ generates a T -point DFT along the temporal direction for every pixel location in image sequence \mathbf{x} . Fourier transform appears to be an attractive choice for temporal sparsity in cardiac MRI for several reasons. It is a simple, global model that does not require any additional information about the signal. It can also be viewed as a method that automatically selects static and dynamic partitions in an image sequence. For instance, a temporal DFT for any pixel in the static region will have just one nonzero component. However, temporal DFT may not be sparse for the pixels in dynamic regions, especially those with sharp amplitude variations, which may have all the DFT coefficients to be nonzero. Therefore, although temporal DFT performs very well in many cases, it does not fully exploit the temporal structure.

Since temporal variations are linked with changes in the spatial domain across different frames and dependencies among neighboring pixels, a temporal transform that adapts to the underlying spatial variations can provide a more effective model for the temporal structure. One such adaptive transform can be constructed using inter-frame motion.

Motion-adaptive spatio-temporal regularization (MASTeR)

Inter-frame motion plays an integral role in modern video compression schemes (e.g., MPEG and H.264 codecs) (22, 23). The fundamental insight is that inter-frame motion provides an effective way to predict neighboring frames from one another. In standard video compression, we divide a video sequence into disjoint groups of frames in which we usually designate one frame as the reference frame and remaining as prediction frames. Starting with the frame after the reference frame, we estimate motion between every frame and its previous neighbor and encode the motion-compensated residuals (constructed by subtracting the original frame from its prediction) using some spatial transform. At the decoder, the reference frame and motion-compensated residuals are used to reconstruct all the frames in the group.

In dynamic MRI, physical changes (e.g., a beating heart in cardiac imaging) govern the transformation between any two adjacent images. Therefore, inter-frame motion provides an efficient model for the underlying temporal structure. However, video compression principles are not directly applicable in dynamic MRI. First, a fully sampled reference frame is not readily available in cardiac MRI. To acquire images at a desired temporal resolution in cardiac MRI, we can observe only a small amount of k-space data (i.e., the number of phase-encoding lines) per frame per heartbeat. Although we can generate a reference frame by combining the downsampled k-space data, a fully sampled image at the same temporal resolution cannot be acquired in an accelerated cardiac MRI. This is because the number of cardiac cycles required for filling up the k-space of either one frame

or all of the frames in the cardiac cycle is the same. Second, we do not have motion information readily available during reconstruction.

In the following section, we show that these problems can be circumvented by describing dynamic MRI in the form of a linear dynamical system in which neighboring frames predict each other using motion-adaptive transforms. The underlying inter-frame motion can be estimated and iteratively refined from available data.

Motion-adaptive linear dynamical system

The displacement of image features in space appears as motion across different frames. Suppose the pixel values in a small neighborhood of location (u, v) in \mathbf{x}_i are closest to the pixel values in the neighborhood of location $(u + \Delta u, v + \Delta v)$ in \mathbf{x}_{i-1} . The collection of $(\Delta u, \Delta v)$ for all pixels constitutes so-called *motion vectors*. We use motion vectors to define a transform that approximates \mathbf{x}_i from \mathbf{x}_{i-1} as

$$\mathbf{x}_i = \mathbf{F}_{i-1}\mathbf{x}_{i-1} + \mathbf{f}_i, \quad [8]$$

where \mathbf{F}_{i-1} denotes a *forward motion operator* and \mathbf{f}_i denotes a *forward motion-compensated residual*. \mathbf{F}_{i-1} can be considered an operator that uses motion information to interpolate the pixel values in \mathbf{x}_{i-1} to displaced locations in \mathbf{x}_i . Similarly, we can approximate images in the reverse direction (i.e., \mathbf{x}_i from \mathbf{x}_{i+1}) as

$$\mathbf{x}_i = \mathbf{B}_{i+1}\mathbf{x}_{i+1} + \mathbf{b}_i, \quad [9]$$

where \mathbf{B}_{i+1} denotes a *backward motion operator* and \mathbf{b}_i denotes a *backward motion-compensated residual*. These forward and backward motion operators construct our so-called *motion-adaptive transforms* that use inter-frame motion to represent an image sequence \mathbf{x} in the form of forward and backward motion-compensated residuals \mathbf{f}_i and \mathbf{b}_i , respectively.

We combine the imaging system in Eq. 1 and the motion compensation equations in Eqs. 8 and 9 to write the following motion-adaptive linear dynamical system:

$$\mathbf{y}_i = \mathcal{A}_i\mathbf{x}_i + \mathbf{e}_i \quad [10a]$$

$$\mathbf{f}_i = \mathbf{F}_{i-1}\mathbf{x}_{i-1} - \mathbf{x}_i \quad [10b]$$

$$\mathbf{b}_i = \mathbf{B}_{i+1}\mathbf{x}_{i+1} - \mathbf{x}_i. \quad [10c]$$

To recover the image sequence \mathbf{x} , we solve Eq. 10 by exploiting sparse structures in \mathbf{x}_i , \mathbf{f}_i , and \mathbf{b}_i for all i .

Recovery algorithm

Now we discuss the details of our proposed recovery algorithm: motion adaptive spatio-temporal regularization (MASTeR). MASTeR uses the dynamical system model described in Eq. 10, in

which we need inter-frame motion to define operators \mathbf{F} and \mathbf{B} so that we can recover the image sequence, yet we need images to compute the inter-frame motion. A common approach to mitigate such a problem is to alternately update estimates of the image sequence and inter-frame motion (33, 34). Therefore, we adopt a two-step approach in which we estimate the image sequence with any available motion information and then use the estimated image sequence to refine the motion information. A pseudocode for the recovery algorithm is as follows.

MASTeR consists of the following two-step iterative procedure:

(1) initialization and (2) motion adaptation.

1. **Initialization:** Solve the following spatial ℓ_1 -regularization problem to recover initial image estimates from their respective k-space measurements:

$$\underset{\mathbf{x}}{\text{minimize}} \sum_i \|\mathcal{A}_i \mathbf{x}_i - \mathbf{y}_i\|_2^2 + \tau \|\Psi \mathbf{x}_i\|_1, \quad [6]$$

where Ψ denotes the spatial sparsifying transform.

2. **Motion adaptation:** This step can be further divided into two intermediate steps and repeated multiple times to improve the reconstruction quality.
 - i. *Motion estimation:* Use the reconstructed image sequence to estimate or refine inter-frame motion and define forward and backward motion operators \mathbf{F}_i and \mathbf{B}_i for all i ¹.
 - ii. *Motion compensation:* Solve the following optimization problem following the dynamical system in Eq. 10:

$$\underset{\mathbf{x}}{\text{minimize}} \sum_i \|\mathcal{A}_i \mathbf{x}_i - \mathbf{y}_i\|_2^2 + \alpha \|\mathbf{F}_{i-1} \mathbf{x}_{i-1} - \mathbf{x}_i\|_1 + \beta \|\mathbf{B}_{i+1} \mathbf{x}_{i+1} - \mathbf{x}_i\|_1. \quad [11]$$

A few remarks about MASTeR are in order. During the initialization step, we do not have any motion information; however, a temporal regularization can be easily added to the optimization problem (e.g., a temporal DFT or a static/dynamic partition of the field-of-view). We used ℓ_1 norms with the last two terms in Eq. 11 because of our assumption that motion-compensated residuals \mathbf{f}_i and \mathbf{b}_i are sparse in the image domain. We can easily modify these residual terms to accommodate sparsity in some transform domain, or in the case of dense residuals, we can replace the ℓ_1 norm with an ℓ_2 norm. Regularization parameters τ , α , and β can be adjusted according to the problem.

¹For the boundary frames, we can either couple them and treat them as neighbors (i.e., a periodic video), or we can ignore the forward motion term for the first frame (at $i = 0$) and the backward motion term for the last frame (at $i = T$).

To estimate the inter-frame motion, we can use any of the existing motion estimation or optical-flow estimation schemes (35, 36, 37, 38, 39, 40, 41). Although our algorithm does not depend on any particular motion estimation scheme, we must emphasize that the quality of reconstructed images directly depends on the quality of the motion estimates. Furthermore, since motion estimates come from the reconstructed images and not the original images, the motion estimation scheme should be robust against both noise and aliasing artifacts. In this regard, we found that compared to block-matching algorithms, which do not perform very well, phase-based motion estimation (42) and optical-flow methods (41) provide significantly better results.

Methods

In our experiments, we used breath-held, prospectively-gated, steady-state free precession (SSFP) cardiac MRI scans, following the protocol approved by the Institutional Review Board. We simulated accelerated imaging setup by decimating fully-sampled k-space data from multiple receiver coils according to a desired sampling pattern. We used downsampled k-space measurements to reconstruct the underlying image sequence using MASTeR. We evaluated the performance of MASTeR reconstruction for two in vivo cardiac MRI scan datasets at different reduction factors. We also compared our results against that of k-t FOCUSS with ME/MC (13).

A short-axis MRI scan (images shown in Figure 1) was acquired using a GE 1.5T TwinSpeed scanner (R12M4) with a 5-element cardiac coil and a FIESTA/FastCARD cine SSFP sequence. Scan parameters were selected as follows: TE: 2.0 ms, TR: 4.1 ms, flip angle: 45° , FOV: 350×350 mm, slice thickness: 12 mm, 8 views per segment, 224 phase-encoding lines, 256 read-out samples, and 16 temporal frames. To emulate the estimation of sensitivity maps from a prescan, we acquired a separate scan (which we assume to be a prescan) with identical scan parameters and estimated sensitivity maps as follows: Half of the (high frequency) k-space samples from each coil were removed from the prescan via a smoothing filter followed by an inverse Fourier transform to obtain smoothed images for each coil. To estimate the sensitivity maps, we divided each smoothed coil image by the root-sum-of-squares of all coil images.

A two-chamber view cine MRI scan (images shown in Figure 4) was acquired using a Philips Intera 1.5T scanner (R10.3) with a 5-element cardiac synergy coil and a balanced fast field echo SSFP sequence. Scan parameters were selected as follows: TE: 2.2 ms, TR: 4.4 ms, flip angle: 45° , slice thickness: 8 mm, 240 phase-encoding lines, 200 read-out samples, and 16 temporal frames. To simulate perfectly registered sensitivity maps, we estimated them from the same data. Although this approach introduces a positive bias in the signal-to-noise ratio of measurements, it eliminates errors that may arise because of the misregistration of sensitivity profiles.

In our experiments, we primarily used a 2-D Cartesian downsampling pattern with a fully sampled low-frequency region and a randomly sampled high-frequency region. To achieve a desired reduction factor, we constructed the downsampled measurements by selecting eight low-frequency

phase-encoding lines around the center of the k-space and the remaining lines at random from the high-frequency region, according to a standard Gaussian distribution. We would like to point out that although we employed the sampling pattern with dense sampling in the low-frequency region, our algorithm does not impose any such restriction on the sampling pattern.

We reconstructed MR image sequences from the downsampled k-space data using MASTeR. We used NESTA toolbox (27) to solve the ℓ_1 -norm minimization problems in [6] and [11]. For the initialization, we solved Eq. 6 using wavelet transform on each frame in the sequence as the spatial sparsifying transform Ψ . For the subsequent motion adaptation iterations, we estimated inter-frame motion from the reconstructed images using phase shifts of their CWT coefficients, updated motion-operators \mathbf{F} and \mathbf{B} , and solved Eq. 11. We coupled the boundary frames such that the forward motion operator for the first frame (at $i = 1$) used the last frame and the backward motion operator for the last frame (at $i = T$) used the first frame during motion estimation and compensation steps. We performed three motion-adaptation iterations of MASTeR for the results presented in this paper.

We used 2-D dual-tree complex-wavelet transform (DT-CWT) (43) as the spatial transform because it provided significantly better images compared with the commonly used orthogonal wavelets. We also used DT-CWT coefficient for estimating inter-frame motion, due to the fact that a local displacement (motion) in the image domain appears as a phase shift in the CWT coefficients (42). The DT-CWT is a redundant, nearly shift-invariant wavelet transform, which decomposes each image into directional, multiscale subbands. Each scale of the wavelet tree produces two complex-valued lowpass and six complex-valued bandpass subimages. A benefit of this redundancy is that local displacements in the image domain cause predictable changes in the wavelet coefficients. In particular, a phase shift of a complex coefficient in each bandpass subimage is approximately linearly proportional to a local displacement in the input image in a certain direction. Starting with the CWT coefficients of two images at the coarsest scale, we can estimate a local displacement vector for every subpixel in the lowpass subimage at that scale using phase shifts of respective coefficients from all the bandpass subimages. We pass the estimated displacement field to the next scale by interpolating and scaling it up by two, where each subpixel at the coarser scale would correspond to four subpixels at the next scale. At the next scale, we start with the interpolated displacement field and use phase shifts of the coefficients at that scale to further refine the displacement field. In this manner, we use a coarse-to-fine refinement strategy to produce a displacement field for each pixel. A MATLAB implementation of MASTeR, along with scripts for the DT-CWT and motion estimation, is available at <http://users.ece.gatech.edu/~sasif/dynamicMRI>.

To compare the results of MASTeR and k-t FOCUSS with ME/MC (13), we implemented iterative reweighted least-squares problem for k-t FOCUSS algorithm with multiple receiver coils using conjugate gradient (CG) method. We selected the regularization parameters for each dataset such that the RMS error between the original and reconstructed sequence is minimized. We selected

the error threshold for CG termination as 10^{-6} and allowed the CG method to run for a maximum of 200 iterations. To report the best possible results for k-t FOCUSS, we recorded the RMS error at every CG iteration and selected the CG estimate with the minimum RMS error. We generated a reference frame by taking average of six images out of 16 reconstructed images. We identified these (almost static) frames in the diastole phase by visually inspecting all the images in each dataset. We used the generated reference frame for the motion estimation and compensation steps in k-t FOCUSS with ME/MC. We performed two iterations of motion-estimation and motion-compensated residual reconstruction with three reweighting iterations each, which provided us overall good performance with k-t FOCUSS with ME/MC.

Results

Short Axis dataset: Figure 1 illustrates the comparison of MASTeR and k-t FOCUSS with ME/MC for the short axis MRI dataset at acceleration factors 4 and 8. Figure 1(a) shows frames 1, 8, and 13 (from left to right) out of the 16 frames in the sequence, calculated from the fully sampled k-space data. The region of interest (ROI), enclosed by the white square box, is the heart region where most of the changes occur. Figure 1(b) presents cropped and zoomed ROI from the three frames in (a). Figures 1(c) and (d) present MASTeR reconstructions at reduction factors 4 and 8, respectively. The first row shows reconstructed images, and the second row shows five times amplified differences between the original and reconstructed images. The results for k-t FOCUSS with ME/MC at reduction factors 4 and 8 are presented in Figures 1(e) and (f), respectively.

The MASTeR reconstruction shows significant improvement over the k-t FOCUSS with ME/MC reconstruction at both reduction factors. MASTeR reconstructions consistently contain less random noise than k-t FOCUSS with ME/MC reconstructions. More importantly, preservation of sharp myocardial edges at high reduction factors, critically important for clinical interpretation of ventricular dynamics, is clearly superior in the MASTeR reconstruction. This perhaps may be best observed in the sharply reduced residual errors practically everywhere along the endo- and epicardial borders, but most prominently visible in the frames (8 and 13) with fastest systolic and diastolic myocardial motion. Furthermore, k-t FOCUSS with ME/MC reconstructions contain a number of aliasing artifacts (visible in bright smooth regions), while the MASTeR reconstructions are much cleaner.

In Figure 2, we illustrate similar observations in three temporal slices taken from selected dynamic locations in the original image sequence. Figures 2(c)–(f) present MASTeR and k-t FOCUSS with ME/MC results. We observe that the MASTeR reconstructions follow temporal variations very closely whereas k-t FOCUSS with ME/MC results are noisy and tend to lose fine details. White arrows in Figure 2(f) illustrate such regions where k-t FOCUSS with ME/MC results show artifacts and fail to follow the temporal variations accurately, whereas MASTeR remains close to the ground truth.

A quantitative comparison of MASTeR and k-t FOCUSS with ME/MC for a range of reduction factors is presented in Figure 3. We evaluated the performance of both methods in terms of signal-to-error ratio (SER) in dB, defined as

$$\text{SER} = 10 \log_{10} \frac{\|\mathbf{x}\|_2^2}{\|\mathbf{x} - \hat{\mathbf{x}}\|_2^2},$$

where \mathbf{x} and $\hat{\mathbf{x}}$ denote the original images (constructed from full k-space data) and reconstructed images, respectively. Solid lines in Figure 3 denote SER over the ROI and dashed lines denote SER over the entire image. SER curves show that MASTeR outperforms k-t FOCUSS with ME/MC at all the reduction factors with SER gains in the range of 4–6 dB.

Two-chamber results: Figures 4 presents in similar fashion comparisons of the reconstruction results of MASTeR and k-t FOCUSS with ME/MC for the two-chamber MRI dataset at reduction factors 6 and 10. Figure 4(a) presents frames 1, 3, and 9 (from top to bottom) out of total 16 frames, constructed from fully sampled k-space data. Figure 4(b) shows the ROI in the three frames. Figures 4(c) and (d) present MASTeR reconstructions at $R = 6$ and $R = 10$, and Figures 4(e) and (f) present k-t FOCUSS with ME/MC results at $R = 6$ and $R = 10$, respectively. At both reduction factors the MASTeR reconstructions have significantly better image quality than k-t FOCUSS with ME/MC. Even though levels of random image noise appear fairly low in all reconstructions shown from this dataset, levels of structured noise are clearly lower in MASTeR compared with k-t FOCUSS with ME/MC. This finding is consistent with our qualitative observations and quantitative SER measurements in the short-axis scan. Moreover, delineation of the mitral valve (of clinical importance for left ventricular valve function assessment) is still adequate at reduction factor $R = 10$ with MASTeR, while the k-t FOCUSS with ME/MC reconstruction has lost most of the image details at this location at this acceleration factor (white arrows in Figure 4(f)).

Figure 5 illustrates three temporal slices from the two-chamber dataset. Figures 5(c)–(f) present MASTeR and k-t FOCUSS with ME/MC reconstruction results. We observe a phenomenon similar to the one observed in Figure 2: MASTeR reconstructions follow temporal variations very closely, but k-t FOCUSS with ME/MC results tend to lose the fine details. The white arrows in Figure 5(f) illustrate the regions where original temporal information is lost.

Discussion

Source of improvement in MASTeR

The fundamental difference between the motion-based temporal models of MASTeR and k-t FOCUSS with ME/MC is that instead of modeling the inter-frame motion with respect to a single reference frame and reconstructing resultant motion-compensated residuals, we modeled the temporal dependencies within neighboring frames in the form of a linear dynamical system and recon-

structed the image sequence using motion-adaptive transforms. We believe that the main source of improvement for MASTeR is this difference in the temporal models. Because even if we generate a good reference frame from the available k-space data, that reference frame may fail to provide a good correspondence for all the other frames in the sequence. We observed this in our experiments on the two-chamber MRI scan where the fine details that were absent in the reference frame also vanished in the k-t FOCUSS with ME/MC reconstructions.

We support this claim by comparing k-t FOCUSS with ME/MC and a variant of that in which we replaced the reference frame-based motion-compensated residuals terms with the motion-adaptive transforms from MASTeR. We call this variant k-t FOCUSS with MASTeR. In both the methods, the initial estimate for the image sequence is identical and is computed by solving k-t FOCUSS (i.e., a least-squares problem with iteratively reweighted temporal-DFT). For the motion-compensation step, k-t FOCUSS with ME/MC solves the following least-squares problem with iterative reweighting:

$$\underset{\Delta \mathbf{x}}{\text{minimize}} \|\mathcal{A}\Delta \mathbf{x} - \mathbf{y}\|_2^2 + \lambda \|\mathbf{W}\mathcal{F}_t\Delta \mathbf{x}\|_2^2, \quad [12]$$

where $\Delta \mathbf{x}$ denotes motion-compensated residuals for the entire image sequence with respect to a reference frame, \mathcal{F}_t denotes a temporal-DFT operator, and \mathbf{W} denotes a diagonal matrix that is used for iterative reweighting. In contrast, k-t FOCUSS with MASTeR solves the following least-squares problem with iterative reweighting:

$$\underset{\mathbf{x}}{\text{minimize}} \|\mathcal{A}\mathbf{x} - \mathbf{y}\|_2^2 + \lambda \|\mathbf{W}\mathcal{M}\mathbf{x}\|_2^2, \quad [13]$$

where \mathbf{x} denotes the image sequence, \mathbf{W} denotes a diagonal reweighting matrix, and \mathcal{M} denotes a motion-compensation operator that uses the forward and the backward motion operators, \mathbf{F}_i and \mathbf{B}_i , to compute the respective motion-compensated differences: $\mathbf{f}_i = \mathbf{F}_i\mathbf{x}_i - \mathbf{x}_{i+1}$ and $\mathbf{b}_i = \mathbf{B}_i\mathbf{x}_i - \mathbf{x}_{i-1}$, for each image \mathbf{x}_i in the sequence \mathbf{x} and stacks them on top of one another. In fact, [13] uses iterative reweighting to approximately solve the following ℓ_1 norm problem of the MASTeR (also presented in [11]):

$$\underset{\mathbf{x}}{\text{minimize}} \|\mathcal{A}\mathbf{x} - \mathbf{y}\|_2^2 + \lambda \|\mathcal{M}\mathbf{x}\|_1. \quad [14]$$

We used identical procedure for optimizing regularization parameters and for iterative reweighting, while solving [12] and [13].

We followed the experimental setup described in the Methods section and compared the reconstructions for MASTeR, k-t FOCUSS with ME/MC, and k-t FOCUSS with MASTeR. The results are presented in Figure 6 (for short-axis scan at reduction factors 6 and 10) and Figure 7 (for two-chamber scan at reduction factors 10 and 12). The results show that, under identical settings of recovery framework, the motion-adaptive model outperforms reference frame-based residual re-

construction. The results for k-t FOCUSS with MASTeR are distinctly better than those of k-t FOCUSS with ME/MC; they are less noisy and preserve the fine details in the reconstructions that are lost in k-t FOCUSS with ME/MC. The results for MASTeR are still superior to those of k-t FOCUSS with MASTeR, which can be due to the use of ℓ_1 norm instead of iteratively reweighted ℓ_2 norm and the use of spatial regularization instead of temporal regularization for the initialization.

Comparison of motion estimation schemes

Motion estimation is a central component of our method, and we desire a robust motion estimation scheme that can perform well with noisy, distorted images. Although we can use any motion estimation scheme in MASTeR framework, we found that CWT phase-based motion estimation performed significantly better than block-matching and overlapped block-matching schemes in our experiments.

In Figure 8 we present an experiment where we reconstructed a short-axis MRI scan at reduction factor $R = 8$ using MASTeR. In the initialization step, we estimated each image by solving [6] using DT-CWT as the sparse spatial transform Ψ . The second column in Figure 8 presents the ROIs of the reconstructed images, which are blurry and contain several artifacts. We used three different schemes for estimating motion: phase shifts of CWT coefficients (in the third column), overlapped block-matching (in the fourth column), and standard block-matching (in the last column). The results clearly show that CWT-based motion estimation scheme is more robust than block matching and overlapped block matching schemes in this setting.

We would like to point out that if we add temporal regularization (e.g., temporal-DFT) in the initialization step, the quality of initial reconstruction improves and OBM-based motion estimation scheme works well. However, we have presented these result to justify the reason for using CWT-based motion estimation scheme in our experiments, in which block-matching based schemes did not perform very well.

Conclusion

We have presented a new recovery algorithm (MASTeR) for highly accelerated dynamic MRI. MASTeR, which uses motion-adaptive transforms to model the temporal sparsity in images, was demonstrated to successfully recover cardiac MR images for a range of acceleration factors. It provided images with consistently superior spatial and temporal resolutions and signal-to-error ratios compared to k-t FOCUSS with ME/MC. The source of improvement in MASTeR over k-t FOCUSS with ME/MC is the motion-adaptive temporal model, where instead of modeling the inter-frame motion with respect to a single reference frame and reconstructing resultant motion-compensated residuals, we reconstructed images using a linear dynamical system that employs motion-adaptive transforms for modeling temporal dependencies between adjacent frames in forward and backward

directions. Our results show that it is feasible to recover high-quality dynamic cardiac MR images with an acceleration factor up to $R = 10$ using MASTeR.

References

1. Pruessmann K, Weiger M, Scheidegger M, Boesiger P, SENSE: Sensitivity encoding for fast MRI. *Magnetic Resonance in Medicine* 1999;42(5):952–962.
2. Kyriakos WE, Panych LP, Kacher DF, Westin C, Bao SM, Mulkern RV, Jolesz FA, Sensitivity profiles from an array of coils for encoding and reconstruction in parallel (SPACE RIP). *Magnetic Resonance in Medicine* 2000;44(2):301–308.
3. Sodickson DK, Manning WJ, Simultaneous acquisition of spatial harmonics (SMASH): Fast imaging with radio-frequency coil arrays. *Magnetic Resonance in Medicine* 1997;38(4):591–603.
4. Griswold MA, Jakob PM, Heidemann RM, Nittka M, Jellus V, Wang J, Kiefer B, Haase A, Generalized autocalibrating partially parallel acquisitions (GRAPPA). *Magnetic Resonance in Medicine* 2002;47(6):1202–1210.
5. Madore B, UNFOLD-SENSE: A parallel MRI method with self-calibration and artifact suppression. *Magnetic Resonance in Medicine* 2004;52(2):310–320.
6. Brummer ME, Moratal-Pérez D, Hong C, Pettigrew RI, Millet-Roig J, Dixon WT, Noquist: Reduced field-of-view imaging by direct fourier inversion. *Magnetic Resonance in Medicine* 2004;51(2):331–342.
7. Kellman P, Epstein FH, McVeigh ER, Adaptive sensitivity encoding incorporating temporal filtering (TSENSE). *Magnetic Resonance in Medicine* 2001;45(5):846–852.
8. Tsao J, Boesiger P, Pruessmann KP, k-t BLAST and k-t SENSE: Dynamic MRI with high frame rate exploiting spatiotemporal correlations. *Magnetic Resonance in Medicine* 2003; 50(5):1031–1042.
9. Hamilton LH, Fabregat JA, Moratal D, Ramamurthy S, Lerakis S, Parks WJ, Sallee III D, Brummer ME, PINOT: Time-resolved parallel magnetic resonance imaging with a reduced dynamic field of view. *Magnetic Resonance in Medicine* 2011;65(4):1062–1074.
10. Lustig M, Donoho D, Pauly J, Sparse MRI: The application of compressed sensing for rapid MR imaging. *Magnetic Resonance in Medicine* 2007;58(6):1182–1195.
11. Liu B, Sebert F, Zou Y, Ying L, SparseSENSE: Randomly-sampled parallel imaging using compressed sensing. In: *Proceedings of the 16th Annual Meeting of ISMRM, Toronto, 2008*; p. 3154.
12. Liang D, Liu B, Wang J, Ying L, Accelerating SENSE using compressed sensing. *Magnetic Resonance in Medicine* 2009;62(6):1574–1584.

13. Jung H, Sung K, Nayak K, Kim E, Ye J, k-t FOCUSS: A general compressed sensing framework for high resolution dynamic MRI. *Magnetic Resonance in Medicine* 2009;61(1):103–116.
14. Velikina J, Johnson K, Block K, Samsonov A, Design of temporally constrained compressed sensing methods for accelerated dynamic mri. In: *Proceedings of the 18th Annual Meeting of ISMRM*, Stockholm, 2010; p. 4865.
15. Candès E, Romberg J, Tao T, Robust uncertainty principles: Exact signal reconstruction from highly incomplete frequency information. *IEEE Transactions on Information Theory* 2006;52(2):489–509.
16. Donoho D, Compressed sensing. *IEEE Transactions on Information Theory* 2006;52(4):1289–1306.
17. Chen SS, Donoho DL, Saunders MA, Atomic decomposition by basis pursuit. *SIAM Journal on Scientific Computing* 1999;20(1):33–61.
18. Tropp J, Just relax: Convex programming methods for identifying sparse signals in noise. *IEEE Transactions on Information Theory* 2006;52(3):1030–1051.
19. Candès E, Tao T, Decoding by linear programming. *IEEE Transactions on Information Theory* 2005;51(12):4203–4215.
20. Candès E, Romberg J, Sparsity and incoherence in compressive sampling. *Inverse Problems* 2007;23(3):969–985.
21. Lustig M, Santos J, Donoho D, Pauly J, k-t SPARSE: High frame rate dynamic MRI exploiting spatio-temporal sparsity. In: *Proceedings of the 13th Annual Meeting of the ISMRM*, Seattle, 2006; p. 2420.
22. Wiegand T, Sullivan GJ, Bjontegaard G, Luthra A, Overview of the H.264/AVC video coding standard. *IEEE Transactions on Circuits and Systems for Video Technology* 2003;13(7):560–576.
23. Sullivan GJ, Wiegand T, Video compression—from concepts to the H.264/AVC standard. *Proceedings of the IEEE* 2005;93(1):18–31.
24. Jung H, Ye J, Motion estimated and compensated compressed sensing dynamic magnetic resonance imaging: What we can learn from video compression techniques. *International Journal of Imaging Systems and Technology* 2010;20(2):81–98.
25. Otazo R, Kim D, Axel L, Sodickson DK, Combination of compressed sensing and parallel imaging for highly accelerated first-pass cardiac perfusion MRI. *Magnetic Resonance in Medicine* 2010;64(3):767–776.

26. Golub G, Van Loan C, Matrix Computations. Johns Hopkins University Press, 1996.
27. Becker S, Bobin J, Candès E, NESTA: A fast and accurate first-order method for sparse recovery. *SIAM Journal on Imaging Sciences* 2011;4(1):1–39.
28. Becker S, Candès E, Grant M, Templates for convex cone problems with applications to sparse signal recovery. *Mathematical Programming Computation* 2011;3(3).
29. Boyd S, Vandenberghe L, Convex Optimization. Cambridge University Press, 2004.
30. Figueiredo M, Nowak R, Wright S, Gradient projection for sparse reconstruction: Application to compressed sensing and other inverse problems. *IEEE Journal of Selected Topics in Signal Processing* 2007;1(4):586–597.
31. Hale E, Yin W, Zhang Y, Fixed-Point Continuation for ℓ_1 -minimization: Methodology and Convergence. *SIAM Journal on Optimization* 2008;19(3):1107–1130.
32. Portnaguine O, Bonifasi C, DiBella E, Whitaker R, Inverse methods for reduced k-space acquisition. In: *Proceedings of the 11th Meeting of ISMRM, Toronto, 2003*; p. 481.
33. Park J, Wakin M, A multiscale framework for compressive sensing of video. In: *IEEE Picture Coding Symposium, 2009*; pp. 1–4.
34. Reddy D, Veeraraghavan A, Chellappa R, P2C2: programmable pixel compressive camera for high speed imaging. In: *IEEE Conference on Computer Vision and Pattern Recognition (CVPR), 2011*; pp. 329–336.
35. Jain J, Jain A, Displacement measurement and its application in interframe image coding. *IEEE Transactions on Communications* 1981;29(12):1799–1808.
36. Srinivasan R, Rao K, Predictive coding based on efficient motion estimation. *IEEE Transactions on Communications* 1985;33(8):888–896.
37. Orchard MT, Sullivan GJ, Overlapped block motion compensation: An estimation-theoretic approach. *IEEE Transactions on Image Processing* 1994;3(5):693–699.
38. Horn BK, Schunck BG, Determining optical flow. *Artificial Intelligence* 1981;17(1-3):185–203.
39. Barron JL, Fleet DJ, Beauchemin SS, Performance of optical flow techniques. *International Journal of Computer Vision* 1994;12:43–77.
40. Brox T, Bruhn A, Papenberg N, Weickert J, High accuracy optical flow estimation based on a theory for warping. In: *European conference on computer vision (ECCV), 2004*; p. 25–36.

41. Liu C, Beyond Pixels: Exploring New Representations and Applications for Motion Analysis. Doctor of philosophy, Massachusetts Institute of Technology, 2009.
42. Magarey J, Kingsbury N, Motion estimation using a complex-valued wavelet transform. IEEE Transactions on Signal Processing 1998;46(4):1069–1084.
43. Selesnick I, Baraniuk R, Kingsbury N, The dual-tree complex wavelet transform. IEEE Signal Processing Magazine 2005;22(6):123–151.

List of Figures

- 1 A comparison of MASTeR and k-t FOCUSS with ME/MC for the short-axis MRI scan: frames 1, 8, and 13 (left to right). (a) Conventional full-grid ground truth images from full k-space. (b) Enlarged spatial ROI. Left column: (c) MASTeR reconstruction at $R = 4$ and (e) k-t FOCUSS with ME/MC reconstruction at $R = 4$. Right column: (d) MASTeR reconstruction at $R = 8$ and (f) k-t FOCUSS with ME/MC reconstruction at $R = 8$. Bottom rows in (c)–(f) show difference images that are amplified by a factor of 5. 24
- 2 A comparison of MASTeR and k-t FOCUSS with ME/MC for the short-axis MRI scan: temporal variations. (a) ROI with lines illustrating the three locations for the temporal slices. (b) Temporal profiles in y-t space at three different locations along x direction. Left column: (c) MASTeR and (e) k-t FOCUSS with ME/MC reconstruction at $R = 4$. Right column: (d) MASTeR and (f) k-t FOCUSS with ME/MC reconstruction at $R = 8$. Bottom rows in (c)–(f) show difference images that are amplified by a factor of 5. White arrows point to regions where we see straight lines instead of smooth variations. 25
- 3 SER comparison of the MASTeR (red,+) and k-t FOCUSS with ME/MC (black,×) for the short-axis MRI dataset at different reduction factors. Solid lines represent SER in the region of interest (ROI) and dashed lines show SER over the entire image. 26
- 4 A comparison of MASTeR and k-t FOCUSS with ME/MC for the two-chamber MRI scan: frames 1, 3, and 9 (top to bottom). (a) Conventional full-grid ground truth images from the full k-space. (b) Enlarged spatial ROI. Top rows: (c) MASTeR reconstruction at $R = 6$ and (e) k-t FOCUSS with ME/MC reconstruction at $R = 6$. Bottom rows: (d) MASTeR reconstruction at $R = 10$ and (f) k-t FOCUSS with ME/MC reconstruction at $R = 10$. Bottom rows in (c)–(f) show difference images that are amplified by a factor of 5. White arrows in (f) point to the regions where heart structure is missing in the k-t FOCUSS with ME/MC reconstruction. 27
- 5 A comparison of MASTeR and k-t FOCUSS with ME/MC for the two-chamber MRI scan: temporal variations. (a) ROI with lines illustrating the three locations of the temporal slices. (b) Temporal profiles in y-t space at three different locations along x direction. Left column: (c) MASTeR and (e) k-t FOCUSS with ME/MC reconstruction at $R = 6$. Right column: (d) MASTeR and (f) k-t FOCUSS with ME/MC reconstruction at $R = 10$. Bottom rows in (c)–(f) show difference images that are amplified by a factor of 5. White arrows point to the regions where temporal information is lost in the k-t FOCUSS with ME/MC reconstruction. 28

6	A comparison of MASTeR, MASTeR with k-t FOCUSS, and k-t FOCUSS with ME/MC for the short-axis MRI scan: frames 1, 3, and 9 (top to bottom). (a) Conventional full-grid ground truth images from the full k-space. (b) Enlarged spatial ROI. MASTeR reconstruction at $R = 6$ in (c) and $R = 10$ in (d). k-t FOCUSS with MASTeR at $R = 6$ in (e) and $R = 10$ in (f). k-t FOCUSS with ME/MC reconstruction at $R = 6$ in (g) and $R = 10$ in (h). Bottom rows in (c)–(h) show difference images that are amplified by a factor of 5.	29
7	A comparison of MASTeR, MASTeR with k-t FOCUSS, and k-t FOCUSS with ME/MC for the two-chamber MRI scan: frames 1, 3, and 9 (top to bottom). (a) Conventional full-grid ground truth images from the full k-space. (b) Enlarged spatial ROI. MASTeR reconstruction at $R = 10$ in (c) and $R = 12$ in (d). k-t FOCUSS with MASTeR at $R = 10$ in (e) and $R = 12$ in (f). k-t FOCUSS with ME/MC reconstruction at $R = 10$ in (g) and $R = 12$ in (h). Bottom rows in (c)–(h) show difference images that are amplified by a factor of 5.	30
8	A comparison of different motion estimation schemes with MASTeR. Column 1: ROIs from frames 1,3, and 13 of the short-axis MRI scan. The images are reconstructed from k-space data at $R = 8$. Column 2: Initial results for frame-by-frame reconstruction using ℓ_1 regularization with DT-CWT. Column 3–5: Results after three motion adaptation iterations when we estimated motion using CWT-based method, overlapped block-matching (OBM)-based method, or standard block-matching (BM)-based method, respectively. Bottom rows in each plot show difference images that are amplified by a factor of 5.	31

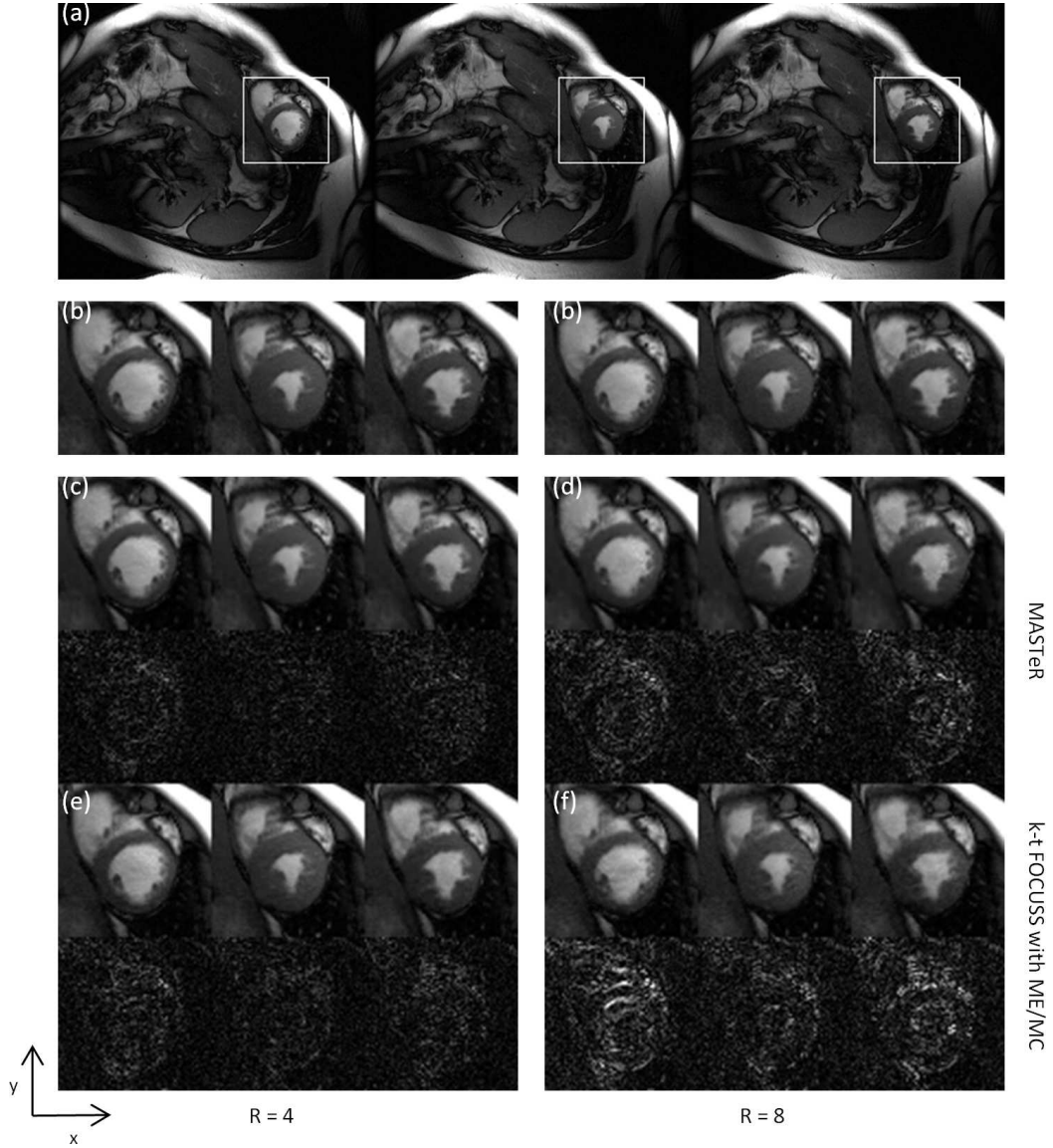


Figure 1: A comparison of MASTeR and k-t FOCUSS with ME/MC for the short-axis MRI scan: frames 1, 8, and 13 (left to right). (a) Conventional full-grid ground truth images from full k-space. (b) Enlarged spatial ROI. Left column: (c) MASTeR reconstruction at $R = 4$ and (e) k-t FOCUSS with ME/MC reconstruction at $R = 4$. Right column: (d) MASTeR reconstruction at $R = 8$ and (f) k-t FOCUSS with ME/MC reconstruction at $R = 8$. Bottom rows in (c)–(f) show difference images that are amplified by a factor of 5.

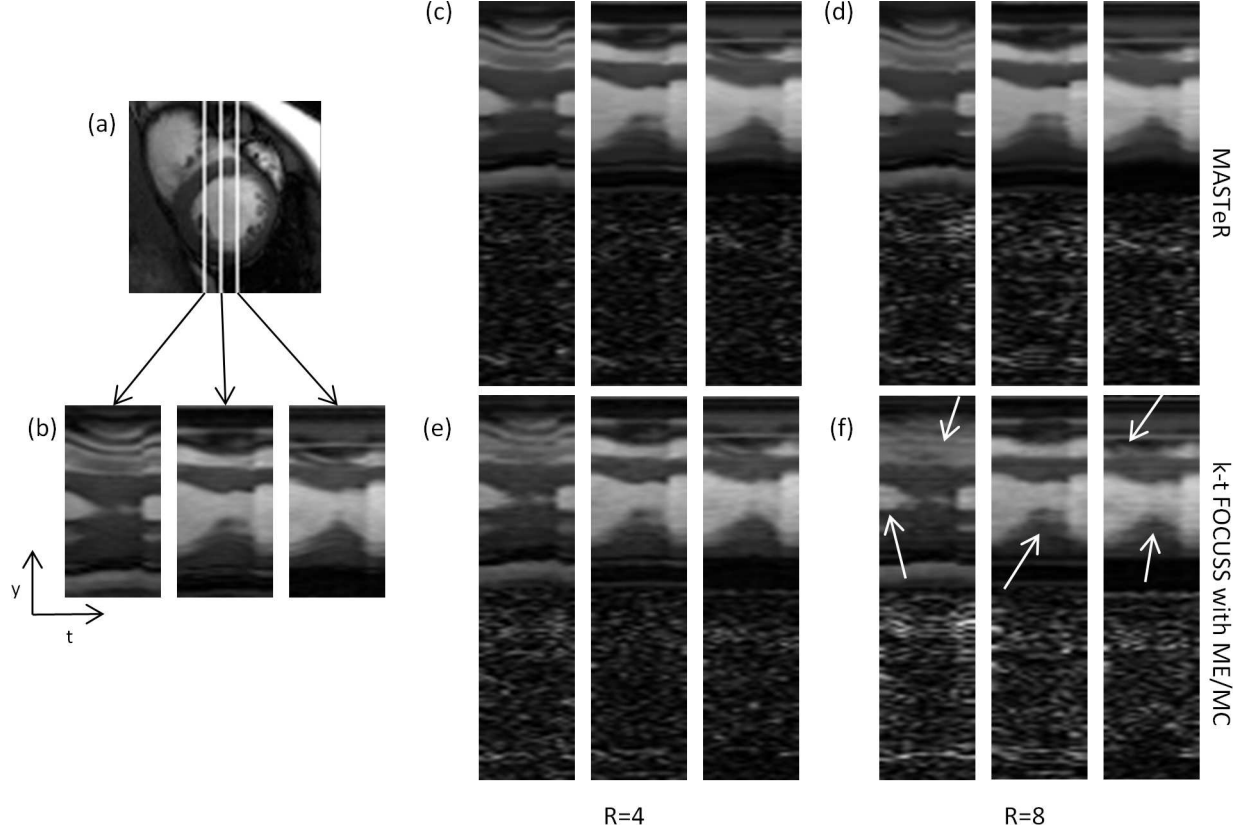


Figure 2: A comparison of MASTeR and k-t FOCUSS with ME/MC for the short-axis MRI scan: temporal variations. (a) ROI with lines illustrating the three locations for the temporal slices. (b) Temporal profiles in y - t space at three different locations along x direction. Left column: (c) MASTeR and (e) k-t FOCUSS with ME/MC reconstruction at $R = 4$. Right column: (d) MASTeR and (f) k-t FOCUSS with ME/MC reconstruction at $R = 8$. Bottom rows in (c)–(f) show difference images that are amplified by a factor of 5. White arrows point to regions where we see straight lines instead of smooth variations.

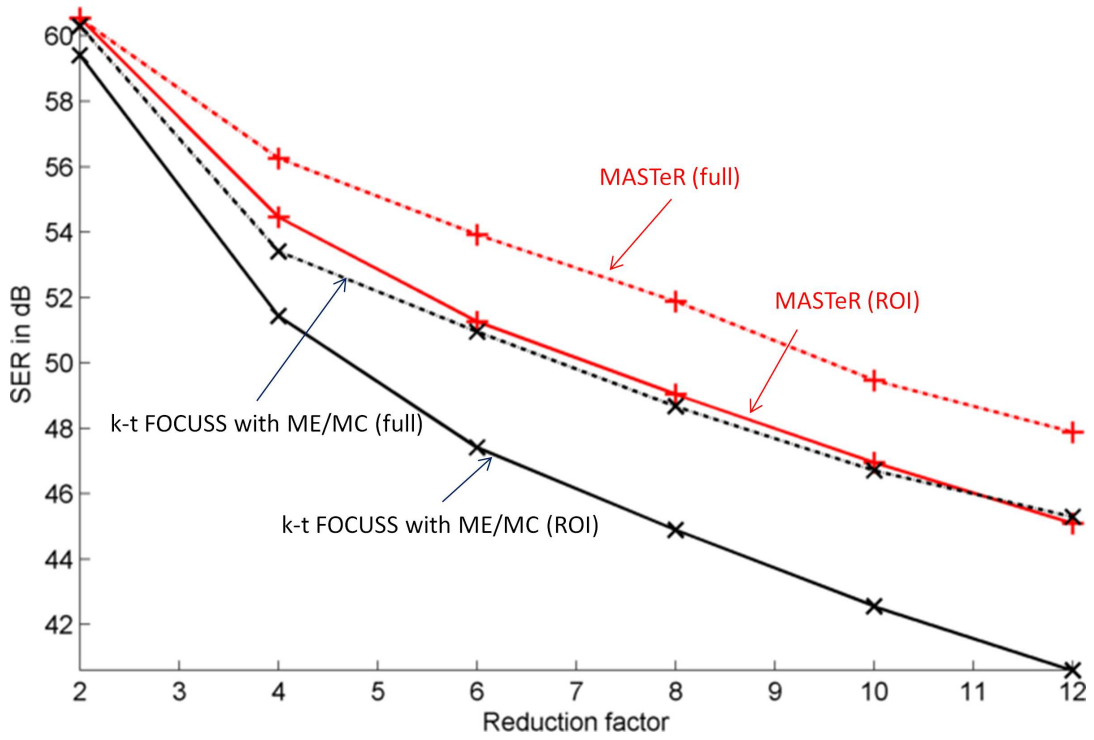


Figure 3: SER comparison of the MASTeR (red,+) and k-t FOCUSS with ME/MC (black,×) for the short-axis MRI dataset at different reduction factors. Solid lines represent SER in the region of interest (ROI) and dashed lines show SER over the entire image.

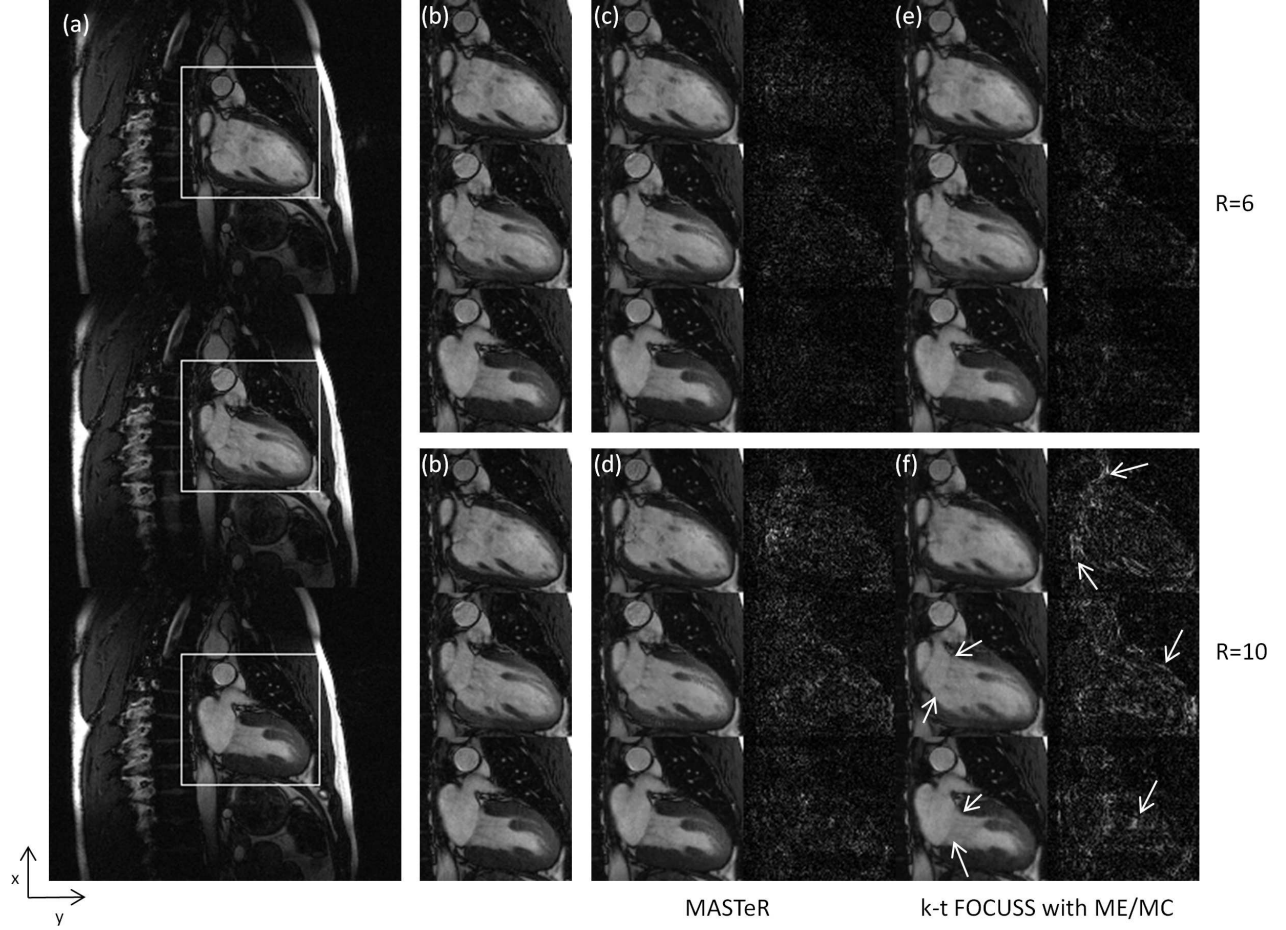


Figure 4: A comparison of MASTeR and k-t FOCUSS with ME/MC for the two-chamber MRI scan: frames 1, 3, and 9 (top to bottom). (a) Conventional full-grid ground truth images from the full k-space. (b) Enlarged spatial ROI. Top rows: (c) MASTeR reconstruction at $R = 6$ and (e) k-t FOCUSS with ME/MC reconstruction at $R = 6$. Bottom rows: (d) MASTeR reconstruction at $R = 10$ and (f) k-t FOCUSS with ME/MC reconstruction at $R = 10$. Bottom rows in (c)–(f) show difference images that are amplified by a factor of 5. White arrows in (f) point to the regions where heart structure is missing in the k-t FOCUSS with ME/MC reconstruction.

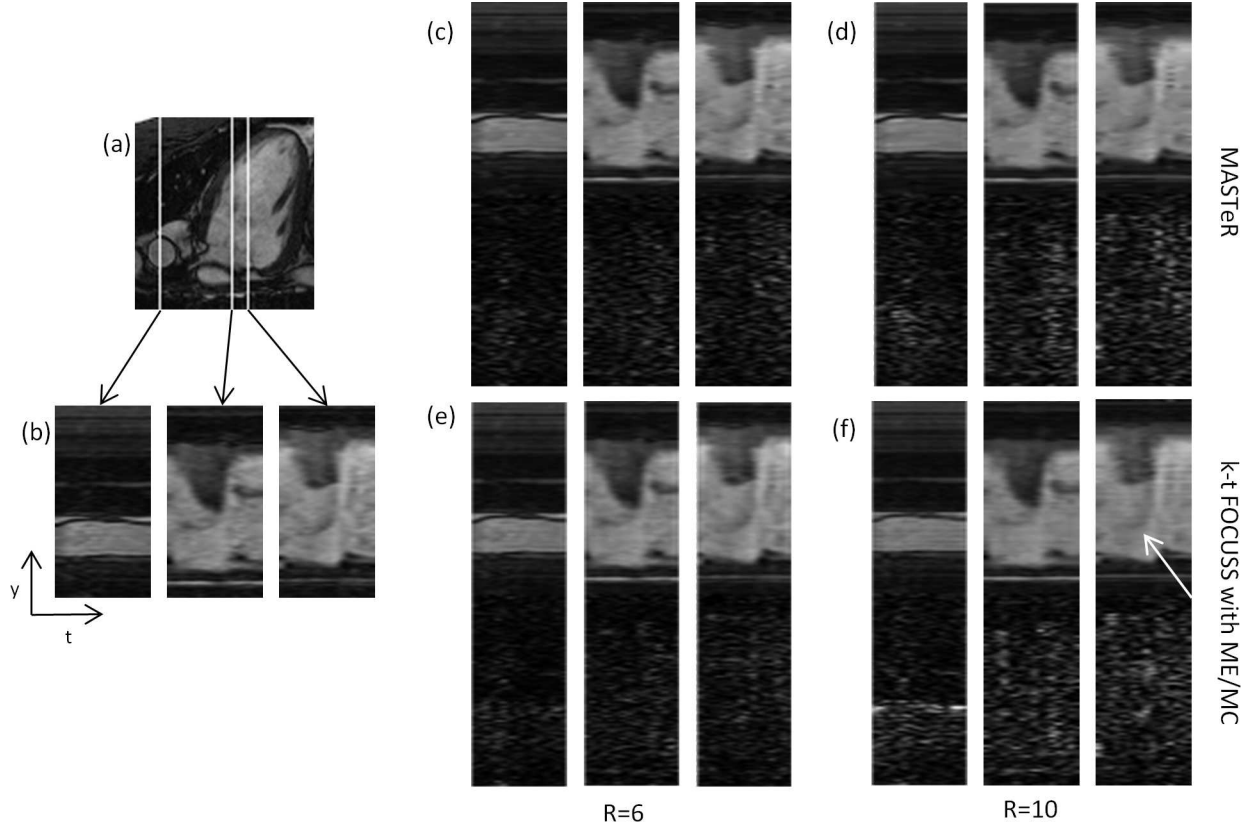


Figure 5: A comparison of MASTeR and k-t FOCUSS with ME/MC for the two-chamber MRI scan: temporal variations. (a) ROI with lines illustrating the three locations of the temporal slices. (b) Temporal profiles in y - t space at three different locations along x direction. Left column: (c) MASTeR and (e) k-t FOCUSS with ME/MC reconstruction at $R = 6$. Right column: (d) MASTeR and (f) k-t FOCUSS with ME/MC reconstruction at $R = 10$. Bottom rows in (c)–(f) show difference images that are amplified by a factor of 5. White arrows point to the regions where temporal information is lost in the k-t FOCUSS with ME/MC reconstruction.

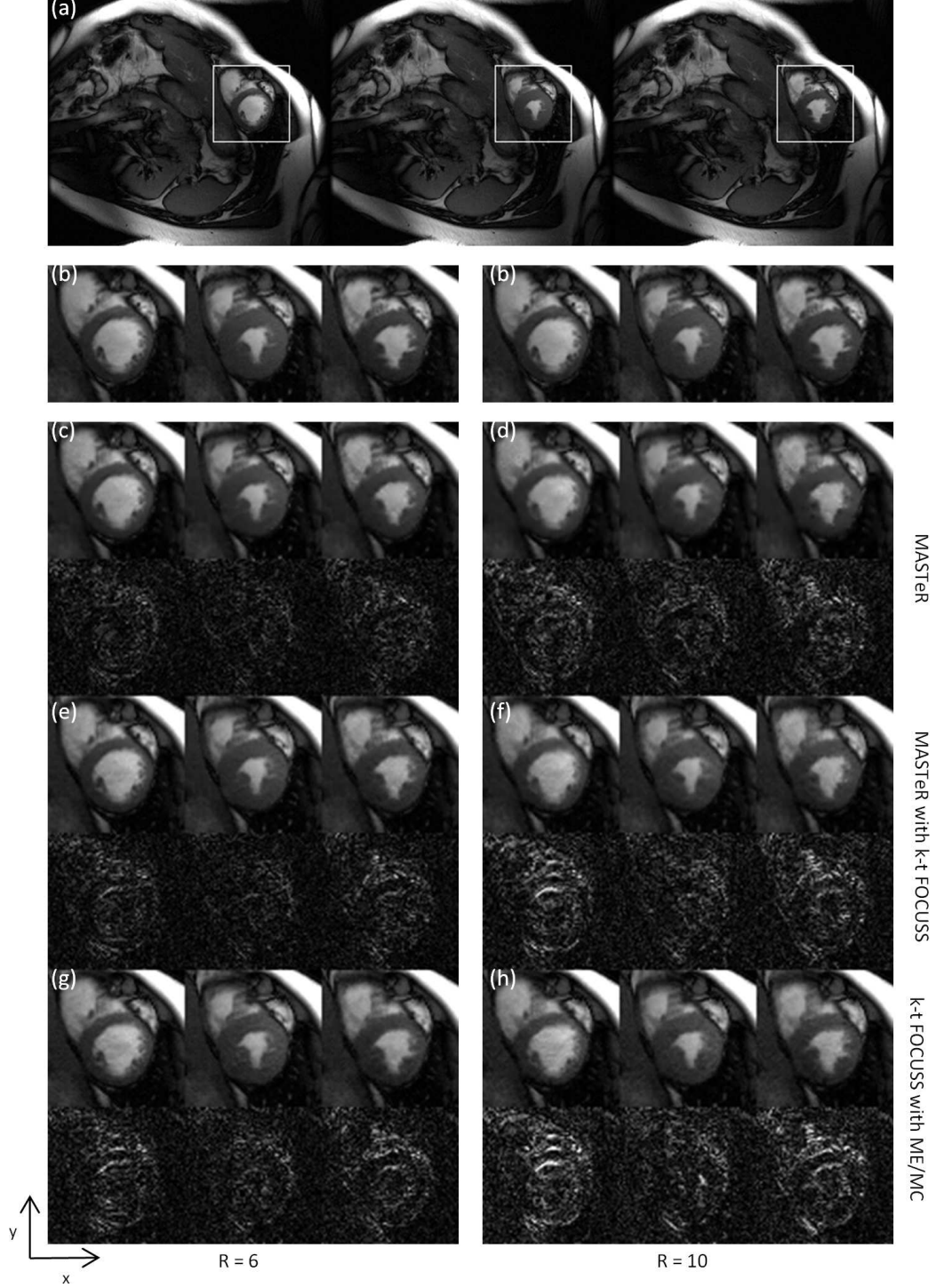


Figure 6: A comparison of MASTeR, MASTeR with k-t FOCUSS, and k-t FOCUSS with ME/MC for the short-axis MRI scan: frames 1, 3, and 9 (top to bottom). (a) Conventional full-grid ground truth images from the full k-space. (b) Enlarged spatial ROI. MASTeR reconstruction at $R = 6$ in (c) and $R = 10$ in (d). k-t FOCUSS with MASTeR at $R = 6$ in (e) and $R = 10$ in (f). k-t FOCUSS with ME/MC reconstruction at $R = 6$ in (g) and $R = 10$ in (h). Bottom rows in (c)–(h) show difference images that are amplified by a factor of 5.

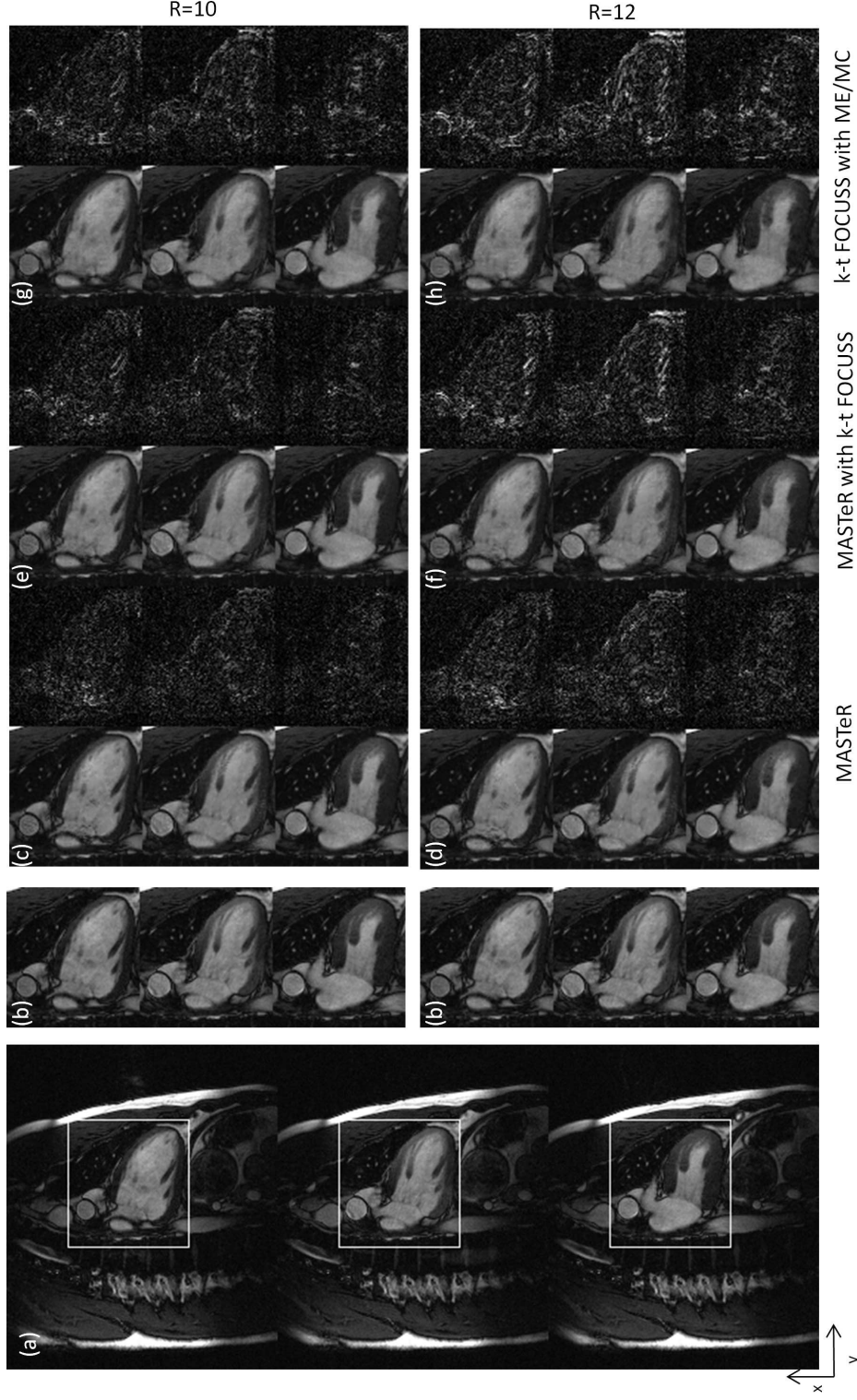


Figure 7: A comparison of MASTeR, MASTeR with k-t FOCUS, and k-t FOCUS with ME/MC for the two-chamber MRI scan: frames 1, 3, and 9 (top to bottom). (a) Conventional full-grid ground truth images from the full k-space. (b) Enlarged spatial ROI. MASTeR reconstruction at $R = 10$ in (c) and $R = 12$ in (d). k-t FOCUS with MASTeR at $R = 10$ in (e) and $R = 12$ in (f). k-t FOCUS with ME/MC reconstruction at $R = 10$ in (g) and $R = 12$ in (h). Bottom rows in (c)–(h) show difference images that are amplified by a factor of 5.

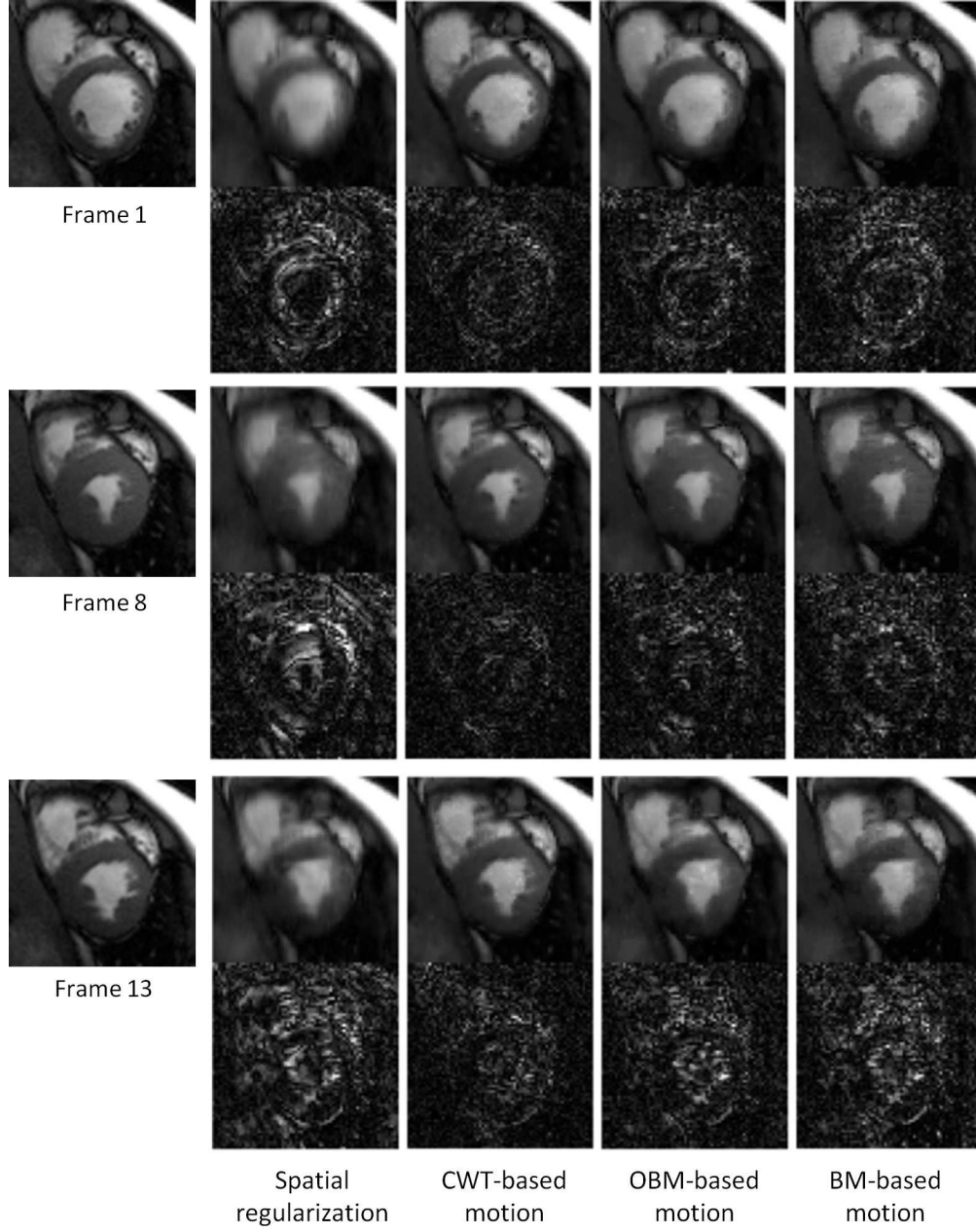


Figure 8: A comparison of different motion estimation schemes with MASTeR. Column 1: ROIs from frames 1,3, and 13 of the short-axis MRI scan. The images are reconstructed from k-space data at $R = 8$. Column 2: Initial results for frame-by-frame reconstruction using ℓ_1 regularization with DT-CWT. Column 3–5: Results after three motion adaptation iterations when we estimated motion using CWT-based method, overlapped block-matching (OBM)-based method, or standard block-matching (BM)-based method, respectively. Bottom rows in each plot show difference images that are amplified by a factor of 5.